AIAA JOURNAL
Vol. 32, No. 7, July 1994

Navier-Stokes Simulations of Slender Axisymmetric Shapes in Supersonic, Turbulent Flow

Kenneth J. Moran* and Philip S. Beran†
Air Force Institute of Technology, Wright-Patterson Air Force Base, Ohio 45433

Computational fluid dynamics is used to study flows about slender, axisymmetric bodies at very high speeds. Numerical experiments are conducted to simulate a broad range of flight conditions. Mach number is varied from 1.5 to 8 and Reynolds number is varied from 1×10^6/m to 2×10^8/m. The primary objective is to develop and validate a computational methodology for the accurate simulation of a wide variety of flow structures. Accurate results are obtained for detached bow shocks, recompression shocks, corner-point expansions, base-flow recirculations, and turbulent boundary layers. Accuracy is assessed through comparison with theory and experimental data; computed surface pressure, shock structure, base-flow structure, and velocity profiles are within measurement accuracy throughout the range of conditions tested. The methodology is both practical and general: general in its applicability, and practical in its performance. To achieve high accuracy, modifications to previously reported techniques are implemented in the scheme. These modifications improve computed results in the vicinity of symmetry lines and in the base flow region, including the turbulent wake.

Nomenclature

A^+ = near wall region length parameter
C_d = drag coefficient
D = body diameter
e = total internal energy per unit volume
J = Jacobian of the transformation (two-dimensional)
L = body length
N = turbulence model pressure gradient function
P^+ = Clauser-like pressure gradient function (inner formulation)
p = pressure
Re = Reynolds number per unit length
r = radial coordinate
s = distance from nosetip along surface
u = velocity in axial direction
v = velocity in radial direction
x = axial coordinate
$\hat{x}$ = distance from nosetip in axial direction
y = distance normal to surface
Z = turbulence model compressibility function
β^* = Clauser-like pressure gradient function (outer formulation)
ε = coefficient in entropy function
$\hat{\lambda}$ = entropy corrected eigenvalue
ρ = density

Introduction

INCREASINGLY, researchers rely on computational fluid dynamics to ascertain the aerodynamic characteristics of vehicles operating at hypervelocities. Projectiles comprise an important class of these vehicles. Although there have been many calculations for both axisymmetric and finned projectiles (see Ref. 2 for an excellent summary), few investigators have analyzed very high-fineness ratio (L/D) bodies, particularly with respect to modeling stability performance at low angle of attack and turbulent boundary-layer development. There is some evidence that these shapes may exhibit stability characteristics unique to hypersonic flight.[3,4] Two recent research efforts are directly pertinent. The authors of Ref. 4 used an upwind, Euler solver to study the stability of a generic finned missile, and the researchers in Ref. 5 used a Beam-Warming, parabolized Navier-Stokes solver to study turbulent boundary-layer development on long, unfinned shells at low angle of attack.

The primary objective of the current study was to build a computational methodology that is sufficiently general to accurately compute a wide variety of flow structures. At the same time, this method must be both frugal in its computer utilization and accurate in predicting the aerodynamics of long projectiles. These requirements must be met so that the approach can be effectively used to study the stability of long, slender, fin-stabilized missiles. The algorithm chosen to meet the objective achieves second-order spatial accuracy away from points of extrema (e.g., shocks), and will be described later. A practical bent was taken throughout the study; optimizing the computational speed was given a priority, and the memory requirement was reduced whenever possible. As a consequence of fulfilling the primary objective, several variations were made to techniques published by other researchers.

The flight conditions of interest involve both high Mach numbers and high Reynolds numbers. This combination is physically complicated and computationally demanding. The complexity arises from the development of strong curved shock waves, the associated vorticity which is generated, and interaction of this vorticity with the boundary layer. Turbulent transition further complicates the interaction. Additional complexity is added by embedded subsonic flow that quickly expands to supersonic flow. Finally, the flat-base results in sudden flow separation, as well as a large mixing layer and recompression shock in the wake. Each of these phenomenon adds to the computational demands. Strong shocks and boundary-layer interactions make it difficult to apply the correct amount of numerical dissipation. The subsonic flow involves a type change in the governing equations (from hyperbolic to elliptic), and turbulent boundary layers and mixing layers require very small grid spacing to resolve steep gradients. The current research investigates the robustness and accuracy of the basic algorithm for the flight conditions of interest. Specifically, tests are run for Mach numbers ranging from 1.5 to 8, and Reynolds numbers from 1×10^6/m to 2×10^8/m.

Calculations are made on axisymmetric bodies with fineness ratios between 9–23. Both laminar and turbulent conditions are simulated on the forebody and base. Because the ongoing goal of the research is to predict the aerodynamics of both finned and unfinned bodies, the ability of the algorithm to calculate a complete configuration is paramount. To demonstrate this ability, laminar flow is computed on a highly blunted, tangent ogive-cylinder model with a flat base. The fineness ratio is 23, and Mach number is varied from 2 to 7; total drag is compared to experimental tests

Received June 3, 1993; revision received Oct. 21, 1993; accepted for publication Oct. 21, 1993.

*Doctoral Student, Graduate School of Engineering, Department of Aeronautics and Astronautics. Student Member AIAA.

†Assistant Professor, Graduate School of Engineering, Department of Aeronautics and Astronautics. Member AIAA.

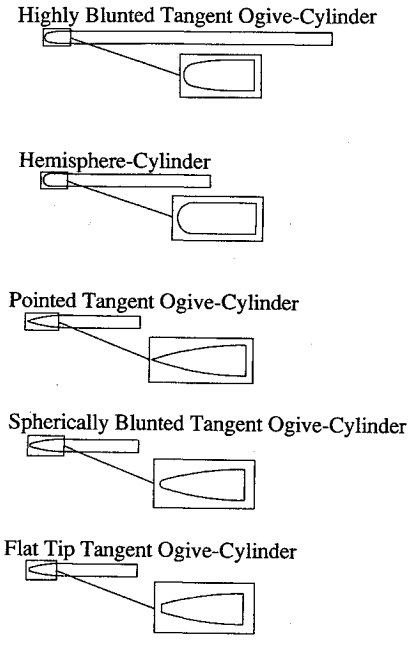

Fig. 1 Experimental /computational models and nosetip shapes.

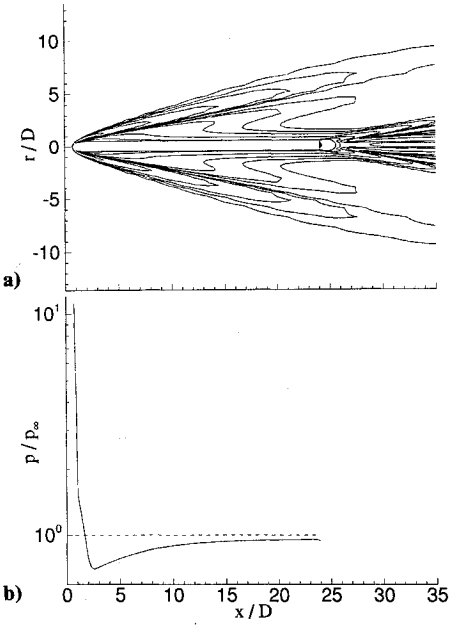

Fig. 2 HBTOC, M_∞ = 3.0, a) pressure contours (5612 grid points) and b) surface pressure.

Table 1 Summary of sensitivity evaluations

Parameter varied	Min-max vaules	Quantity observed	Change in quantity	Tested configuration	Notes
Number of nodes along body	61-121	C_d	4%	HC	Laminar
Number of nodes normal to body	61-181	Pressure one body diam. from surface	0.1%	HC	Laminar
Spacing at sing. line, $\Delta s/D$	0.005-0.04	Tip stagnation pressure	2%	HC	Laminar
Wall spacing, $\Delta y/D$	0.0001-0.001	Tip stagnation pressure	0.1%	HC	Laminar
Wall spacing, $y^+\|_{wall}$	0.6-24.0	$\partial u/\partial y\|_{wall}$	15%	PTOC and BTOC	Turbulent
Entropy func. coefficient, c_1	0.002-0.85	Base stagnation pressure	28%	CFB	Turbulent
Entropy func. coefficient, c_1	0.002-0.85	Integrated base pressure	4%	CFB	Turbulent

of this shape (with fins).[4] Laminar flow is also computed on a hemisphere cylinder, L/D = 14, at Mach 7.78 and compared to the experiments of Ref. 6 These comparisons provide a refined level of flow interrogation to verify the algorithm's accuracy. Then, turbulent flow is computed on pointed, flat, and spherically tipped tangent ogive shells, L/D = 9, at Mach 2.95. Results are compared to both experimental[7,30] and independent computational results.[8] These tests determine the algorithm's ability to accurately predict the influences of upstream effects on boundary-layer development. Finally, turbulent flow is computed for a flat base region and Mach numbers between 1.5–7.0. These results are compared to experimental data reported in Refs. 9–14. The base flow tests are performed to demonstrate the validity and accuracy of the wake region turbulence model, described later.

Computational Approach

Because the future objective is to study the static and dynamic stability traits of high fineness ratio (long and slender) bodies, the methodology's practical and general nature is extremely important. The Navier-Stokes equations are solved with an explicit, time-integration technique, incorporating an upwind, Roe-type, flux-difference splitting (FDS) scheme.[15] In practice, the equations are solved after they are transformed from the physical (r, x) to the computational or generalized (ξ, η) coordinate system. To establish a baseline, an initial assessment of the algorithm is made assuming axisymmetric flow. This provides an appropriate reference point for future investigations using the full, three-dimensional equations.

The geometric singularity associated with axisymmetry poses significant difficulty when employing either two-dimensional or three-dimensional grids. Recent work reported in Ref. 16 proposed two methods of handling this singularity for three-dimensional grids. Both of these methods are explored here, in the context of axisymmetric flow. Some differences were found on both the forebody and base. These will be highlighted in subsequent discussions.

The first procedure reformulates the governing equations, transferring the curvilinear terms to source-like vectors, $\bar{H}$ and $\bar{W}$. For the cylindrical form of the Navier-Stokes equations, which incorporate the axisymmetric assumption, transformation would yield

$$\frac{\partial \bar{U}}{\partial t} + \frac{\partial \bar{E}}{\partial \xi} + \frac{\partial \bar{F}}{\partial \eta} + \bar{H} = \frac{\partial \bar{R}}{\partial \xi} + \frac{\partial \bar{S}}{\partial \eta} + \bar{W} \tag{1}$$

$$\bar{U} = \bar{J}^{-1} U$$

$$\bar{E} = \bar{J}^{-1}(\xi_x E + \xi_r F)$$

$$\bar{F} = \bar{J}^{-1}(\eta_x E + \eta_r F) \tag{2}$$

$$\bar{H} = \frac{1}{r\bar{J}}[\rho v, \rho uv, \rho v^2, (e+p)v]^T$$

E and F are the convective flux vectors in Cartesian coordinates. The explicit forms of E, F and the viscous flux vectors can be found in Ref. 1; $\bar{J}^{-1}$ is computed from the expression

$$\bar{J}^{-1} = x_\xi r_\eta - x_\eta r_\xi \tag{3}$$

Because $\bar{H}$ and $\bar{W}$ are not evaluated on the singular (symmetry) line, they are never singular.

Unlike the approach taken in Ref. 16, which was finite-difference, the current technique implements the discretization of Eq. (1) with the finite-volume methodology. Although the transfomed equation deviates from its integral formulation roots, local physical conservation is addressed when applying Eq. (1) to a cell in physical space by calculating the flux terms and geometric terms at the faces of the cell. The grid points themselves represent the vertices of the cells. This is important at computational boundaries, where the boundary conditions are handled in a manner consistent with a cell interface representing a boundary; boundary conditions are outlined later. The geometric terms (metrics and Jacobian) associated with Eq. (2) are calculated at cell centers from finite-difference expressions, and averaged to obtain values at cell interfaces. This approach is considered a hybrid finite-difference/finite-volume approach by the authors.

For the second procedure, a pure, three-dimensional, finite-volume representation of the geometric terms is utilized. Again Eq. (1) applies, but now

$$\bar{U} = (r\bar{J}^{-1})U$$

$$\bar{E} = (r\bar{J}^{-1}\xi_x)E + (r\bar{J}^{-1}\xi_r)F \tag{4}$$

$$\bar{F} = (r\bar{J}^{-1}\eta_x)E + (r\bar{J}^{-1}\eta_r)F$$

$$\bar{H} = \bar{J}^{-1}[0, 0, -p, 0]^T$$

As before, E and F are the inviscid Cartesian flux vectors, but $\bar{H}$ differs. Expressions for the geometric appearing in Eq. (4) are calculated at cell interfaces from grid cell vertices (grid points). These evaluations are straightforward, and the reader is referred to Ref. 17 for an excellent treatment of the subject.

For both procedures, the viscous terms are centrally differenced, while the convective terms are upwind differenced. Discretization of Eq. (1) is as follows:

$$\bar{U}^{n+1}_{i,j} = \bar{U}^n_{i,j} - \Delta t\left[\left(\hat{\bar{E}}^n_{i+\frac{1}{2},j} - \hat{\bar{E}}^n_{i-\frac{1}{2},j}\right) + \left(\hat{\bar{F}}^n_{i+\frac{1}{2},j} - \hat{\bar{F}}^n_{i-\frac{1}{2},j}\right)\right.$$
$$\left. - \left(\bar{R}^n_{i+\frac{1}{2},j} - \bar{R}^n_{i-\frac{1}{2},j}\right) - \left(\bar{S}^n_{i+\frac{1}{2},j} - \bar{S}^n_{i-\frac{1}{2},j}\right) + \bar{H}^n_{i,j} - \bar{W}^n_{i,j}\right] \tag{5}$$

The exact forms of $\hat{\bar{E}}$ and $\hat{\bar{F}}$ are provided later. The convective fluxes are typically determined at cell interfaces in two ways, using either a Monotonic Upwind Scalar Conservation Law

Table 2 Summary of comparison between computation and theory or experiment

Basis of comparison	Comparison with	Configuration	Case description	Difference in result	Notes
Tip stagnation pressure	Inviscid, perf. gas theory	HC	Case 5 (see Table 3)	0.5%	Laminar
Streamwise velocities	Law of wall/ law of wake[24]	PTOC and BTOC	$y^+ \approx 1$ (see Table 2)	0.2%	Turbulent
Surface pressure	Experiment[30]	PTOC and BTOC	121 nodes along body and $y^+ \approx 1$	4% (max) 1% (avg)	Turbulent
Integrated base pressure	Experiment[9–14]	CFB	31 nodes along base and $c_1 = 0.85$	10% (max) 1% (avg)	Turbulent

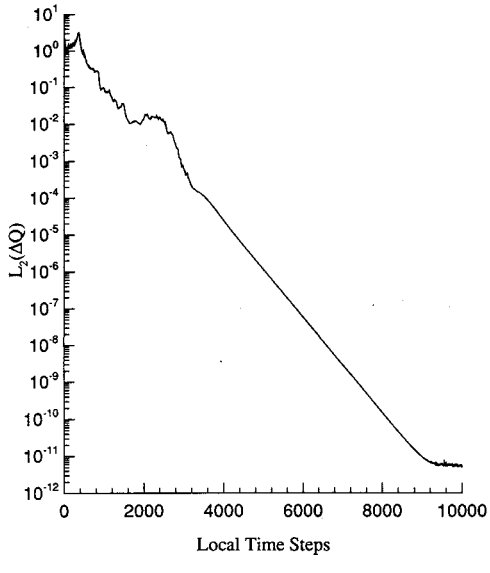

Fig. 3 Convergence history with local time stepping (forebody/base combination).

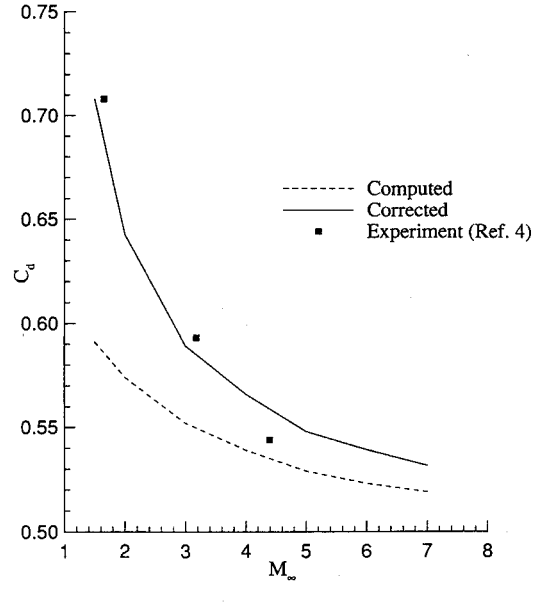

Fig. 4 Total drag coefficient.

(MUSCL) or non-MUSCL extrapolation. In the MUSCL approach, cell-centered values of primitive, conserved, or characteristic variables are extrapolated to the interfaces; fluxes and numerical fluxes are obtained from these quantities. The non-MUSCL approach, on the other hand, calculates the fluxes and numerical fluxes at cell interfaces directly from cell-centered information. The current scheme uses the non-MUSCL technique. The authors chose a non-MUSCL approach for this study because its implementation is more efficient and more straightforward than the MUSCL form.

The explicit, second-order formulation employed for this study is based on the work of Yee[18] and Harten.[19] The formulation is a modification of Roe's first-order algorithm, and has been referred to in the literature as a modified-flux scheme. This scheme achieves second-order accuracy by applying Roe's first-order FDS algorithm to a modified inviscid flux. The flux is chosen so that the scheme is second-order accurate in regions of smoothness and first-order at points of extrema (e. g., shocks). When using finite-volume expressions for the geometric terms, the convective flux in the ξ-coordinate direction at the $(i + 1/2, j)$ interface is approximated by

$$\hat{\bar{E}}_{i+\frac{1}{2},j} = \frac{1}{2}\Big[(r\bar{J}^{-1}\xi_x)_{i+\frac{1}{2},j}(E_{i+1,j}+E_{i,j}) + (r\bar{J}^{-1}\xi_r)_{i+\frac{1}{2},j}(F_{i+1,j}+F_{i,j}) + (r\bar{J}^{-1})_{i+\frac{1}{2},j} R_{i+\frac{1}{2},j}\Phi_{i+\frac{1}{2},j}\Big] \quad (6)$$

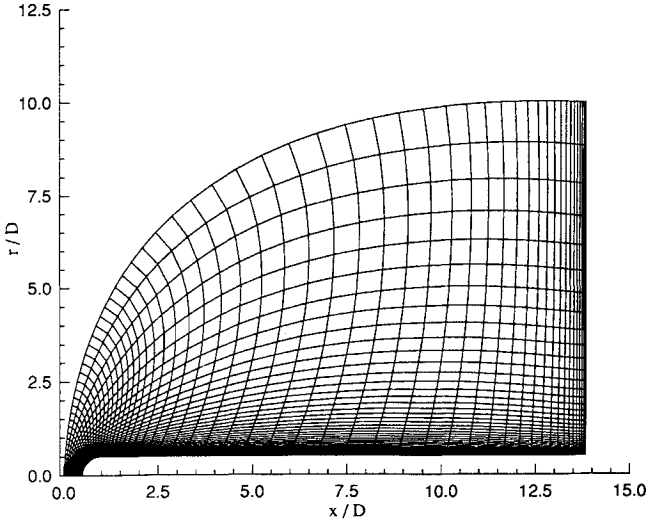

Fig. 5 Grid for hemisphere cylinder, case 1.

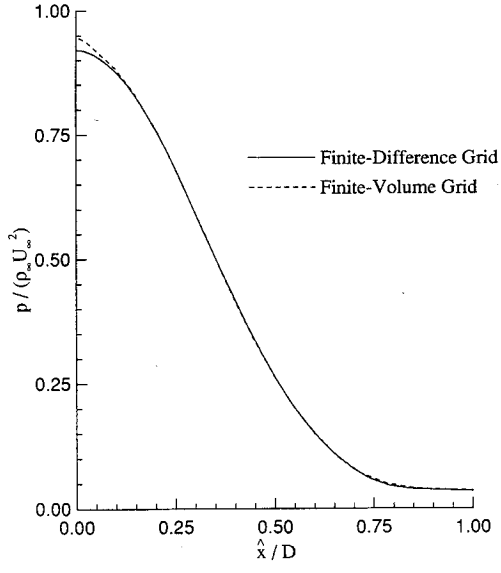

Fig. 6 Aberration in surface pressure at the stagnation point.

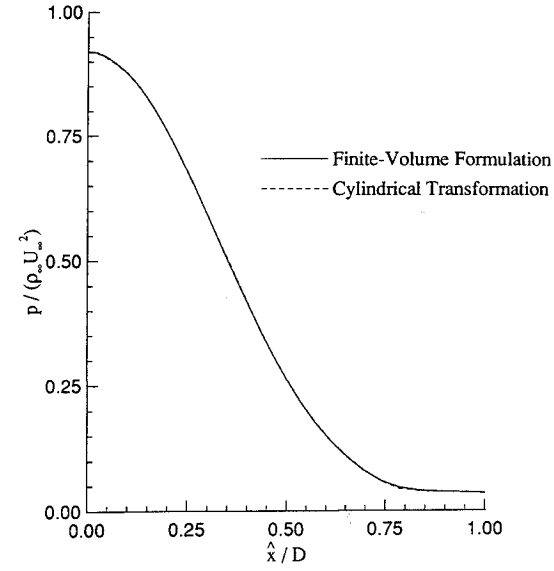

Fig. 7 Comparison of surface pressure for modified solution procedures.

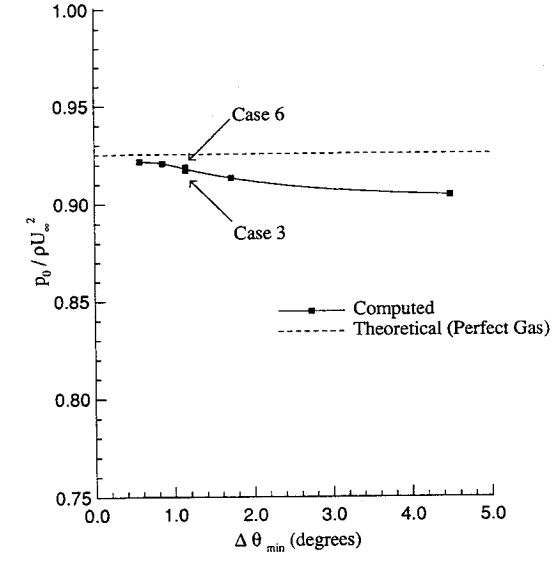

Fig. 8 Stagnation pressure from grid refinement tests.

A similar expression is obtained for the hybrid finite-difference/finite-volume approach; only the terms involving metrics differ. Φ acts to limit the characteristic variables, thereby providing higher accuracy. The current study uses the minmod limiter; details regarding the development and implementation of the limiter are contained in Refs. 18 and 19. Φ also provides an entropy correction when the magnitude of the eigenvalues become small. Entropy correction prevents nonphysical solutions from developing, as is well documented in the literature.[18–20] The form of the entropy corrected eigenvalues put forth by Harten[19] is

$$\hat{\lambda} = \begin{cases} \dfrac{\lambda^2+\varepsilon^2}{2\varepsilon} & |\lambda| < \varepsilon \\ |\lambda| & |\lambda| \geq \varepsilon \end{cases} \quad (7)$$

where the proper value of ε can be very sensitive to the geometry and the flowfield structure. Three relations were tested in this study: a constant value, proposed by Harten[19]; a value proportional to the contravariant velocities, proposed by Yee,[18] and a value proportional to the second derivative of the pressure, suggested by Palmer and Ventkatapathy.[16] Because the purpose for this correc-

tion is to avoid the computation of nonphysical solutions, the functions were evaluated on this basis. In particular, for the current class of flows (axisymmetric, external, supersonic) avoiding aberrations near the singular line was the primary criterion used. Other factors considered were impact on convergence to steady state and dissipation side effects. Entropy correction was not applied near the body surface to avoid adverse effects on the boundary layer. Lin[32] showed undesirable results when the function proposed by Yee was used in the boundary layer. Lin put forth a modification to allow the function to be used globally. However, the current authors feel that the natural viscosity of the fluid prevents nonphysical solutions near the body without the addition of an entropy function.

By far, the most accurate and robust function, for the flows explored herein, was obtained when ε was proportional to the contravariant velocities.

$$\varepsilon = c_1 (|U_c| + |C_c|) \tag{8}$$

where c_1 was varied from 0.2 to 1.0. Equation (8) contains a small modification to Yee's original formula, which included a contribution from the tangential velocity with respect to the grid interface (V_c). The best results were calculated with $c_1 = 0.2$; results were judged best because nonphysical solutions were avoided, convergence was not impeded, and smearing due to the added dissipation was minimized. A value of 0.2 was used for all calculations reported in this study (except base flow experiments, explained later). Some difficulties were still encountered near stagnation points. These are also expounded upon in a later section.

Boundary Conditions

Due to the supersonic condition at both the inflow and outflow, the boundary conditions were very straightforward. At the inflow, freestream conditions were applied, and at the outflow, extrapolation was used. For the body surfaces, no slip was applied, zero normal pressure gradient was used, and either constant wall temperature or an adiabatic wall was used. Finally, symmetry was enforced using ghost cells for the finite-volume grid, and second-order expressions for the finite-difference grid.

Turbulence Modeling

The well known and widely used Baldwin-Lomax turbulence model[21] is incorporated for the forebody boundary-layer simulations. Two modifications, however, proved important. The first changes the Van Driest damping factor to account for compressibility and pressure gradients.[22–24] The near-wall region, denoted by A^+, is redefined as

$$A^+ = 26 \cdot N \cdot Z \tag{9}$$

The nondimensional distance 26 is the incompressible value for a smooth, nonporous, flat plate,[24] N is the pressure gradient contribution, and Z is the compressibility contribution.

$$N = \left[11.8\left(\frac{\rho_e}{\rho_w}\right)P^+ - 1\right]^{-\frac{1}{2}} \qquad Z = \left(\frac{\rho_w}{\rho}\right)^{\frac{1}{2}}\left(\frac{\mu}{\mu_w}\right)$$

$$P^+ = \left(\frac{\mu_e}{\rho_e^2}\right)\frac{(dp_e/dx)}{(\tau_w/\rho_w)^{\frac{3}{2}}} \tag{10}$$

The second alteration improves the two coefficients in the outer region, C_{cp} and C_{kleb}. According to Granville, the following functional forms better match the law of the wake.[25]

$$C_{\text{kleb}} = \frac{2}{3} - \frac{0.01312}{0.1724 + \beta^*} \qquad C_{cp} = \frac{3 - 4C_{\text{kleb}}}{2C_{\text{kleb}}(2 - 3C_{\text{kleb}} + C_{\text{kleb}}^3)} \tag{11}$$

$$\beta^* = \frac{y_{\max}}{(\tau_w/\rho)^{\frac{1}{2}}}\frac{dU_e}{dx}$$

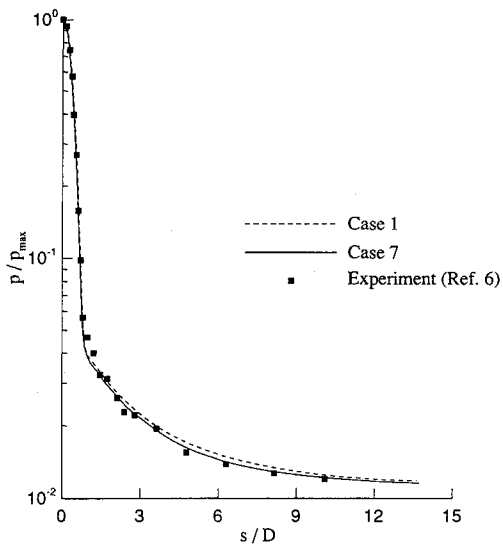

Fig. 9 Surface pressure, case 1 and case 7.

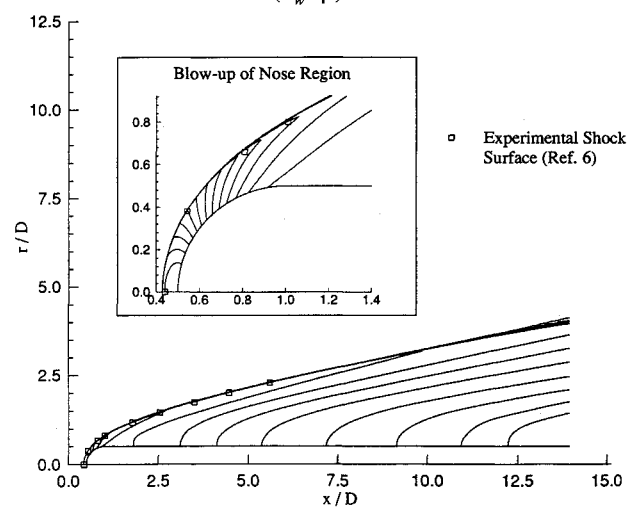

Fig. 10 Pressure contours, case 7.

Table 3 Summary of numerical experiments for hemisphere cylinder

Case	Grid size	$\Delta(s/D)_{\min}$	$\Delta\theta_{\min}$	Comments
1	61 × 61	0.0390	4.49	$\Delta y/D = 0.001$, finite difference (FD) grid
2	91 × 61	0.0150	1.72	"
3	121 × 121	0.0100	1.15	"
4	121 × 121	0.0075	0.86	"
5	121 × 121	0.0050	0.57	"
6	121 × 181	0.0100	1.15	"
7	121 × 181	0.0100	1.15	$\Delta y/D = 0.0001$, FD grid
8	121 × 181	0.0100	1.15	Global time step (GTS), FD grid
9	121 × 181	0.0100	1.15	FV metrics, GTS, FD grid
10	121 × 181	0.0100	1.15	Adiabatic wall, GTS, FD grid

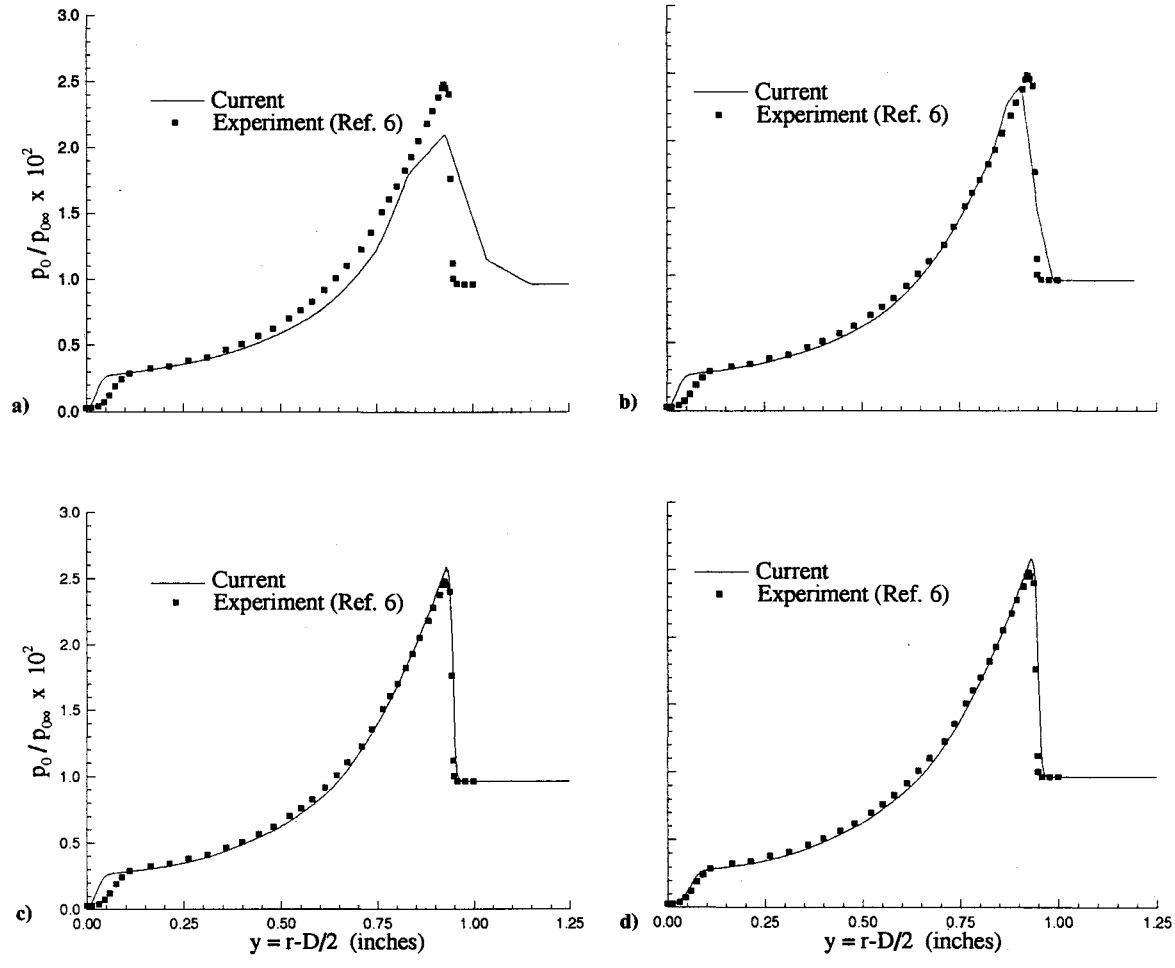

Fig. 11 Impact pressure, $\hat{x}/D = 3$: a) case 1, b) case 3, c) case 7, and d) case 10.

For a flat base with a large, nearly stagnant region, it is difficult to apply a conventional zero equation turbulence model. So, a strictly empirical relation is used to compute turbulent viscosity in the wake. This technique was originally applied to subsonic flow in Ref. 26. We adapt the method and test its validity for supersonic flow in this investigation. Turbulent viscosity is determined locally from

$$\mu_t = \hat{\mu}_t \left(\frac{|\omega|}{|\hat{\omega}|} \right)^{0.2} \tag{12}$$

where $\hat{\mu}_t$ is the maximum viscosity in the boundary layer at the forebody/base juncture, computed from the Baldwin-Lomax model; $\hat{\omega}$ is the vorticity at that point. The researcher of Ref. 26 smoothed the eddy-viscosity with an exponential damping factor. Smoothing was deemed neither desirable nor physical by the current authors, and thus was not pursued in this study. The method has the advantage of speed and low memory requirement. Although highly empirical, the validity of this approach is shown through numerical examples later.

Computer Resources

All grids were obtained using GRIDGEN,[27] an elliptical grid generator developed for Wright Laboratory, Wright-Patterson Air Force Base, Ohio. Both finite-volume grid types (cell interface along singular line), and finite-difference grid types (cell center along singular line) were employed. Surface clustering was employed in the generation of all grids (typical grid, 61×61, for the hemisphere cylinder shown in Fig. 5). Local time stepping was used to accelerate the solution to steady state. The convergence criterion was the reduction of $L_2(\Delta Q)$ by five orders of magnitude. For a turbulent solution, 5 μs of CPU time were required per time step, per node point, on a CRAY Y-MP8. Also, approximately 110 words of memory were required per node point, or 2.4 megawords for the finest grids used (22,000 points).

Results

Numerical simulations were performed for several geometries and flow conditions to assess the general applicability of the methodology developed. Flow over the forebody and flow in the wake were calculated separately and together. In addition, both laminar and turbulent conditions were analyzed over a broad range of Mach numbers. Finally, several different nose-tip shapes (Fig. 1), with varying degrees of bluntness, were investigated.

Accuracy and sensitivity issues are summarized in Tables 1 and 2. Details are highlighted in the sections that follow. Numerical accuracy is judged from comparisons with theoretical solutions for stagnation pressure and velocities in a turbulent boundary layer. Additionally, the effect of the entropy correction parameter on surface pressure is assessed for both the nose and wake regions.

Highly Blunted Tangent Ogive Cylinder, Laminar

This was the longest model used ($L/D = 23$), and was particularly blunt in comparison to other tangent ogive models tested. Its length, highly blunted nose, and flat base made it a demanding choice for full-configuration analysis. To increase the demand on the algorithm, the solution was impulsively started from freestream initial conditions. These conditions were set to match those of the ballistic gun range testing facility at Eglin Air Force Base. A description of the system is given in Ref. 4. This is essentially an open atmosphere system, so standard sea-level conditions were chosen. To provide an unambiguous baseline for subsequent turbulent calculations, strictly laminar flow was simulated on this configuration.

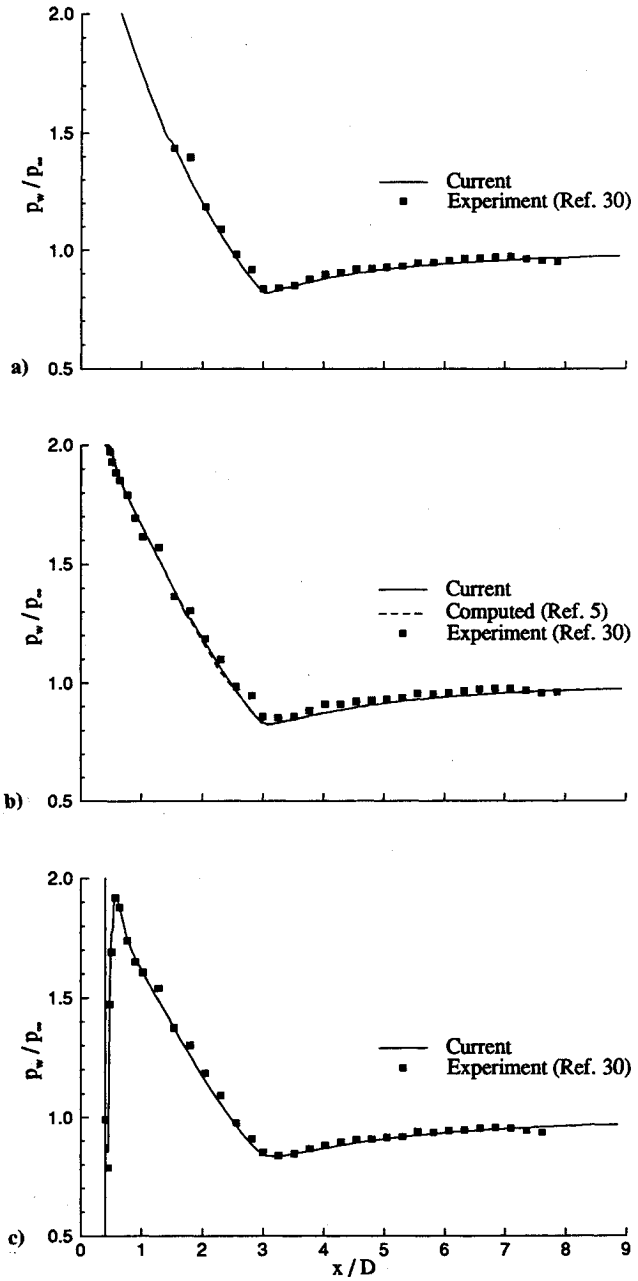

Fig. 12 Surface pressure: a) tip P, b) tip R3, and c) tip F3.

Two techniques dramatically accelerated convergence to steady state. First, the Reynolds number was artificially set to 1×10^{10} at $t = 0$. After the shock wave moved away from the body (outside the boundary layer), the Reynolds number was reset to the correct value. Second, during the transient flow development, a lower limit on density and pressure was used to prevent negative values on the base, typically $\rho_{min} = 0.01\ \rho_\infty$ and $p_{min} = 0.01\ p_\infty$. This additional restriction on the base was continuously enforced, but actually only necessary for the first few hundred iteration from an impulsive start.

The computed solution for $M_\infty = 3$ and $Re = 6.99 \times 10^7/m$ is presented in terms of pressure contours and surface pressure in Figs. 2a and 2b, respectively. The effects of the highly blunted nose are evidenced by the relatively long recovery of surface pressure to the freestream value. The convergence history shows the robustness of the present method (Fig. 3). Total computing time, using the convergence criterion related above, is about 9 min on a CRAY Y-MP8. Finally the total drag (wave, friction, and base) is compared to the drag on the experimental model with fins (Fig. 4). Unfortunately, the base pressure is drastically affected by the existence of fins and turbulent flow.[10,11] Neither turbulent flow nor the presence of fins are accounted for in the computations, thus the comparison is poor. However, if the computed base pressure is replaced by an empirical base pressure which accounts for turbulent flow and the fins,[28] the agreement shown in Fig. 4 is quite good, considering the remaining discrepancy of some turbulent flow on the forebody for the experimental tests.

Hemisphere Cylinder, Laminar

Due to a lack of experimental data, a detailed interrogation of the flowfield was not performed during the earlier full-configuration analysis of the highly blunted, tangent ogive cylinder (HB-TOC). The experimental data for flow over a hemisphere cylinder (HC),[6] provides a more complete basis for evaluating the accuracy of computed solutions both near the body and away from the body. Again laminar flow was assumed in all simulations for this configuration.

The experiment was conducted in the continuous flow, closed return, hypersonic wind tunnel located at the California Institute of Technology. Computed solutions are compared to experimental estimates of shock location, surface pressure, and impact pressure. For the experiment, the reservoir pressure was $2.17 \times 10^6 N/m^2$ ±0.01%, the supply temperature was 645 K ±0.4%, and the Mach number was 7.7 ±1%. At Mach 7.78, the freestream test conditions correspond to $Re = 9.2 \times 10^6/m$. The experimental model was 19.1 mm in diameter (Fig. 1). Measured surface pressure and impact pressure are accurate to within 2%; shock slope and position are accurate to within 3% (Ref. 6).

Except where noted, all solutions were obtained using T_w = 700 K, local time stepping, and the cylindrical transformation [Eqs. (1) and (2)]. Table 3 summarizes the case history of numerical experiments. The grid type [finite-volume (FV) or finite-differ-

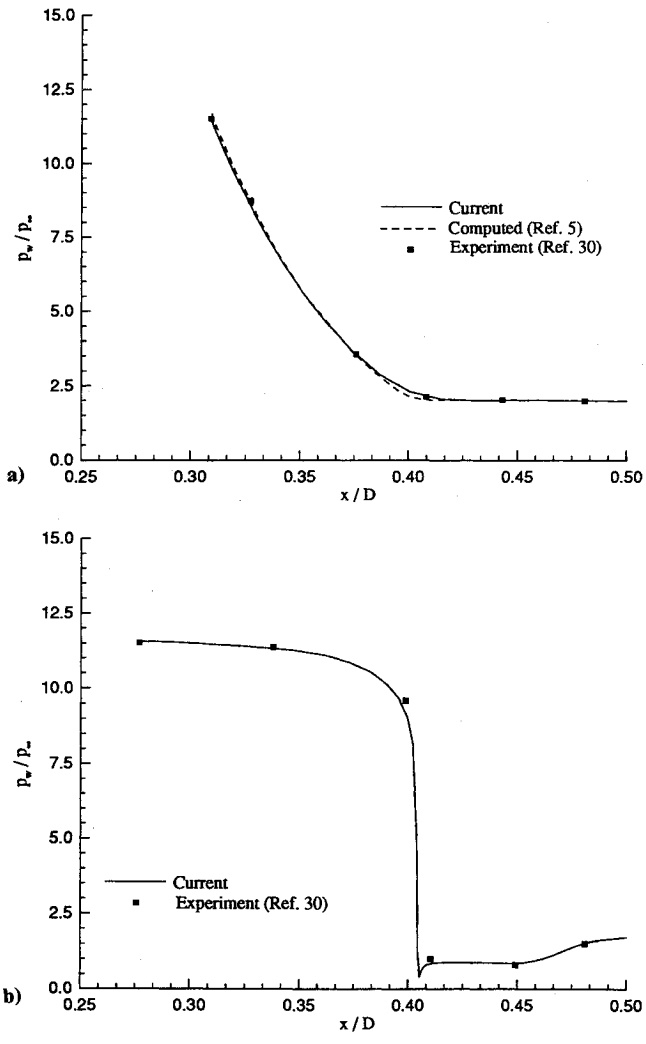

Fig. 13 Nose region surface pressure: a) tip R3 and b) tip F3.

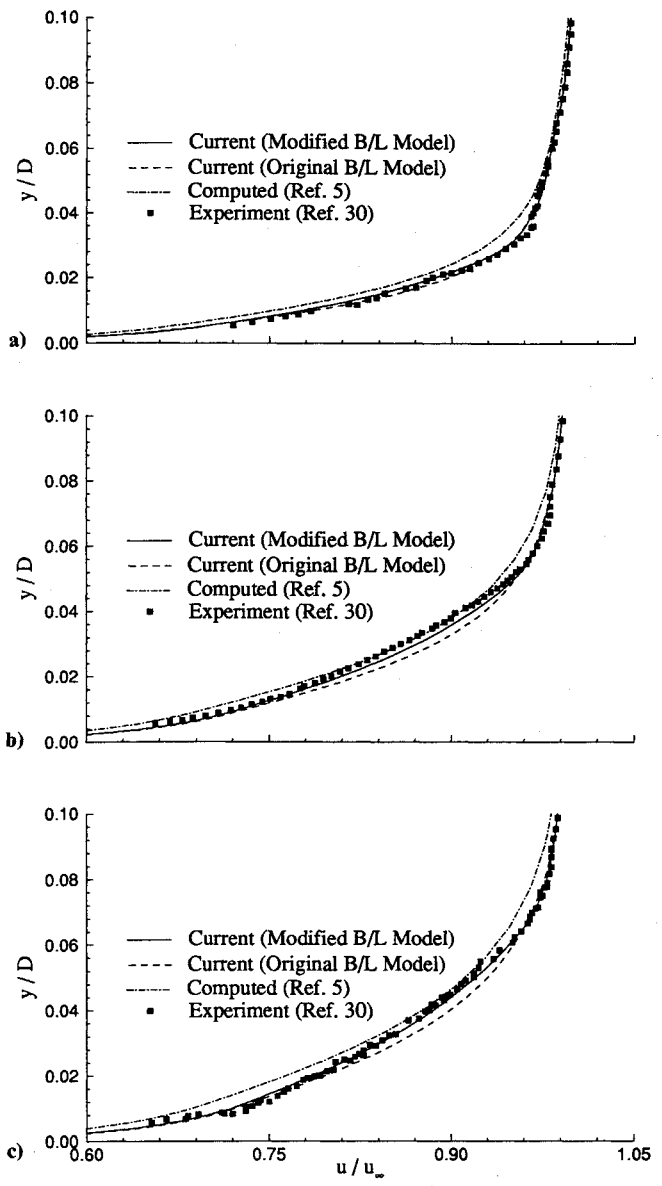

Fig. 14 Velocity profiles, tip R3: a) $x/D = 3.26$, b) $x/D = 5.05$, and c) $x/D = 6.33$.

ence (FD)] had an undesirably large influence on the solution character near the stagnation point. Again, a FV grid has cell interfaces on the symmetry line, while a FD grid has cell centers on the symmetry line. As seen in Fig. 6, the FV grid produced a local aberration in the pressure, manifested as an over prediction in stagnation pressure. It is important to note that this error is not the same as stagnation region distortions reported in the literature as carbuncles.[16,29] This phenomenon did not appear to begin at the shock, and was not accompanied by recirculating flow as with the carbuncle. The entropy function appeared to effectively prevent the carbuncle anomaly. Because similar calculations, using MUSCL extrapolation to achieve higher accuracy,[29] did not demonstrate this error, the authors believe non-MUSCL extrapolation accentuated the geometric singularity when using a FV grid. According to Palmer and Ventkatapathy,[16] the "key to effectively treating the singularity line boundary lies not in boundary conditions themselves, but rather in the proper determination of the metric and flux terms on the singular line." This observation is underscored by the results of this work. A different form of extrapolation (non-MUSCL vs MUSCL) was used in the current scheme, as well as cylindrical vs Cartesian equations. Nonetheless, either technique worked well when using a FD grid (Fig. 7). For the remainder of tests on this geometry, and the rest of the study, a FD grid was employed.

Because the entropy correction function is not used in the boundary layer on the nose and forebody computations, its magnitude primarily affects the solution away from the body. As previously stated, the entropy correction function is made large enough to prevent nonphysical solutions; increases beyond that point affect stagnation pressure less than 0.2%.

The grid-refinement experiments (cases 1–6) are evaluated by examining the stagnation pressure as a function of the node spacing at the surface, $\Delta(y/D)_{min}$, and the node spacing at the singular line, $\Delta\theta_{min}$. The computed stagnation pressure is compared to the value predicted from inviscid, perfect gas theory. The computed stagnation pressure accuracy depends primarily on the grid spacing along the body, near the symmetry line; the error decreases as this spacing decreases. The effect due to spacing at the singular line is shown in Fig. 8. The computed pressure (nondimensional) appears to approach asymptotically the theoretical value of 0.925. The values differ by about 2% for the coarsest grid and less than 0.5% for $\Delta\theta_{min} \approx 0.57$ deg (see Table 2). In contrast, stagnation pressure error is virtually unaffected by grid refinement normal to the body, and varied < 0.1% for the range of spacing tested, $0.0001 \leq \Delta(y/D)_{min} \leq 0.001$ (see Table 1). Although not compared to an exact solution, surface pressure away from the stagnation point exhibits identical sensitivity to grid refinement. A comparison with experiment is shown in Fig. 9 for cases 1 and 7. Agreement within experimental accuracy is achieved. Computed pressure contours illustrate that shock location and shape are also accurately predicted (Fig. 10). A notable exception is the slight over prediction in standoff distance, which the authors attribute to the perfect gas assumption. Finally, impact pressure profiles examined at a station downstream of the nose, $\hat{x}/D = 3$ are in Fig. 11 for cases 1, 3, 7, and 10. Two points highlight the impact pressure profiles. First, as with surface pressure, grid refinement did not appreciably alter the solution near the body. Second, although undocumented by the experiment, an adiabatic wall condition matches the experimental data best. Again, agreement within the experimental accuracy is achieved.

Pointed and Blunted Tangent Ogive Cylinder, Turbulent

The turbulent boundary layer on a projectile or missile is affected by the nose geometry for several reasons. First, the transition to turbulent flow is affected by the higher entropy, lower

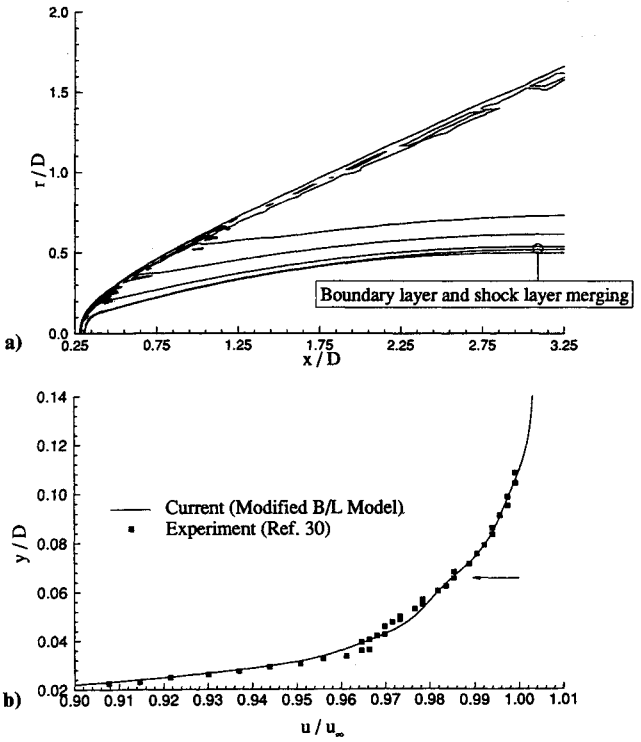

Fig. 15 Vorticity interaction on tip R3: a) vorticity contours and b) velocity profile at $x/D = 3.26$.

Mach number fluid near the stagnation point of blunt noses. Second, the vorticity associated with shock curvature interacts with the boundary layer downstream of the nosetip. Third, for the case of a flat nosetip, the flow separates. Therefore, a series of nose shapes are investigated to evaluate the accuracy of the current algorithm to calculate a developing boundary layer, under differing upstream conditions. Experiments are used for comparison.[30]

The experiments were carried out in the Princeton University 20 × 20 cm, supersonic, high-Reynolds number, blow-down tunnel.[30] The reservoir pressure was $6.8 \times 10^5 N/m^2$ ±1% and the supply temperature was 265 K ±5%. At Mach 2.95 these correspond to $Re = 6.3 \times 10^7/m$. The experimental models were 4.95 cm in diameter and are shown in Fig. 1. To distinguish between the nose shapes, the experimental terminology is adopted; tip P refers to the pointed model, tip F3 refers to the flat nose model, and tip R3 refers to the spherically blunted model.

During the Princeton experiments, the wall temperature remained within 3% of the adiabatic value. Boundary layer transition occurred at $s/D \sim 0.9$–1.5 for tip P, at $s/D \sim 0.7$–1.1 for tip F3, and at $s/D \sim 1.5$–2.5 for tip R3, where s is the distance along the surface from the stagnation point. The accuracy in the surface pressure measurements was ±1.0%. However, variations in the data due to changing stagnation conditions over the duration of the experiments showed a stagnation pressure variance of about ±3%.

Boundary layer transition was not simulated. Rather, a point of transition to a fully turbulent boundary layer was specified. Downstream of this point, the turbulence model was used. These transition points were $s/D = 0.8$, $s/D = 1.0$, and $s/D = 1.7$ for tips F3, P, and R3, respectively. The performance of the algorithm was not adversely affected by the abrupt change in effective viscosity (a small variance was detectable in the pressure at the surface).

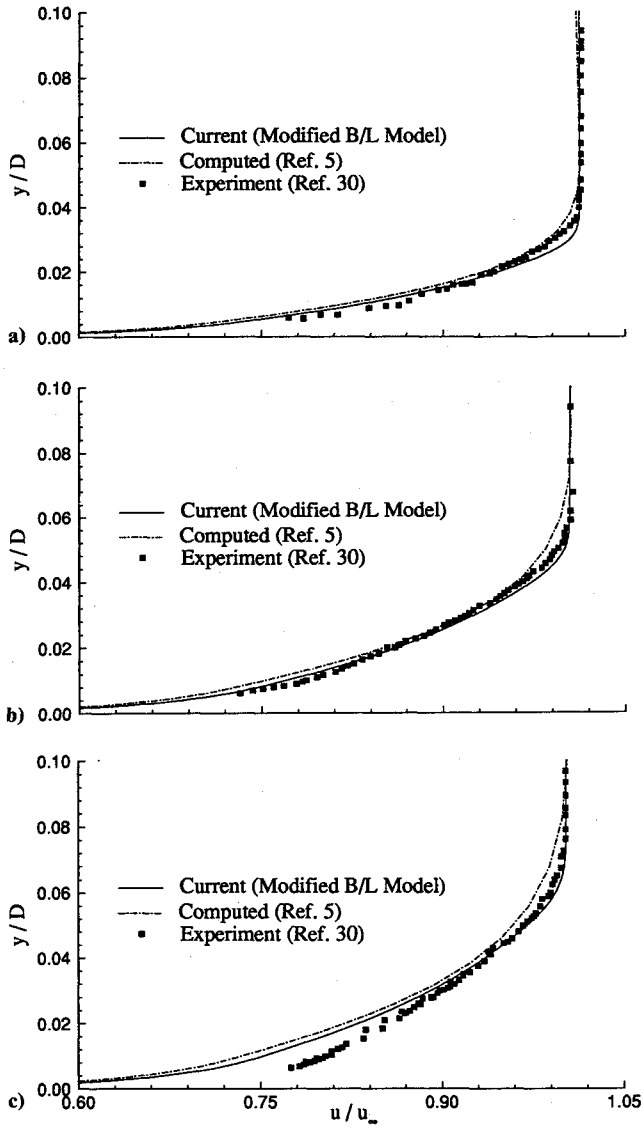

Fig. 16 Velocity profiles, tip P: a) $x/D = 3.26$, b) $x/D = 5.05$, and c) $x/D = 6.33$.

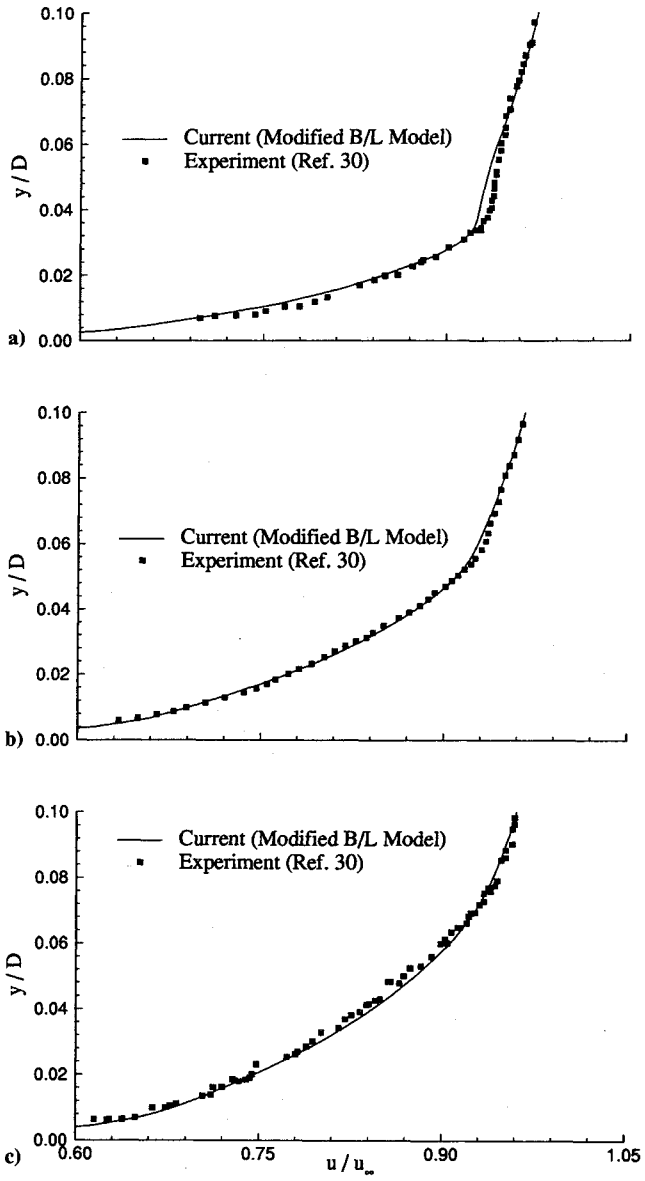

Fig. 17 Velocity profiles, tip F3: $x/D = 3.26$, b) $x/D = 5.05$, and c) $x/D = 6.33$.

It is well known that Roe-type approximate Riemann solvers, which include information about all waves, can accurately calculate boundary layers in relatively coarse mesh.[33] Therefore, the grid refinement analysis concentrated on the appropriate spacing nearest the body. For turbulent flow computations, the velocity gradients at the surface varied significantly with grid spacing normal to the surface. However, there were no further variations for grid refinement equivalent to $y^+_{wall} < 1$. (See Table 1; y^+ is the distance from the body surface nondimensionalized using shear velocity.) For $y^+_{wall} \approx 1$ the time-averaged velocities in the turbulent boundary layer are compared to the law of the wall/law of the wake. Velocity error throughout the boundary layer is ±0.2% (see Table 2). This is an appropriate comparison, as the Baldwin-Lomax turbulence model was developed to produce law of the wall/law of the wake profiles.

Surface pressures are computed to within experimental accuracy; comparison is shown in Fig. 12 for tips P, R3, and F3. Also shown are the computations of Ref. 5 for tip R3. Figure13 shows

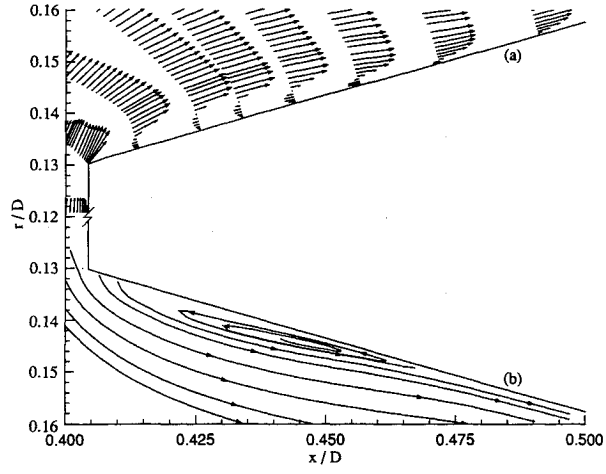

Fig. 18 Separation on flat nosetip (F3): a) velocity vectors and b) streamlines.

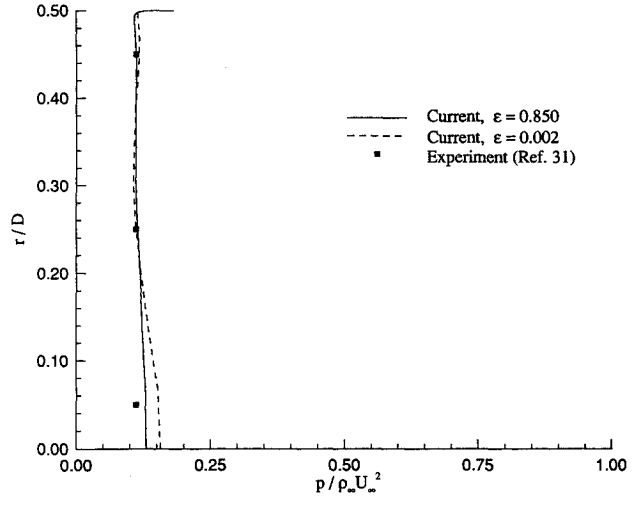

Fig. 19 Base pressure, $M_\infty = 2$.

the comparison for the first six pressure taps on the nose of tips R3 and F3. The current calculation shows expansion on tip F3 slightly sooner than the experimental data. The pressure rise due to the recompression shock is accurately predicted, however.

Because boundary-layer development is sensitive to a pressure gradient, the modifications to the turbulence model described earlier proved important in this region. Figure14 shows computed velocity profiles for tip R3 using the original Baldwin-Lomax turbulence model and the modified model. The computations of Ref. 5 are also included for comparison. In Ref. 5 the original Baldwin-Lomax model and a transition model (polynomial function) were used; transition was initiated at $s/D \approx 0.5$, and fully turbulent conditions were achieved at $s/D \approx 1.5$. Results from Ref. 5 agree qualitatively with the current results using the original Baldwin-Lomax model. The authors attribute differences between the current calculations using the original model and those of Ref. 5 to differences in transition modeling. Significant improvement with the modified Baldwin-Lomax model is visible.

The boundary layer thickens quickly downstream of the transition point. This is discernible from the vorticity contours (Fig. 15a). The vorticity associated with the bow shock interacts with the rapidly thickening boundary layer near the ogive-cylinder shoulder. The vorticity contours clearly depict that the shock layer and boundary layer merge. The arrow in Fig. 15b shows the approximate point above the surface where this merger can be seen for $x/D = 3.26$. The small depression in the velocity profile is further evidence of the interaction.

Computed profiles from the modified model are also shown for tips P and F3 in Figs. 16 and 17, respectively. Excellent agreement

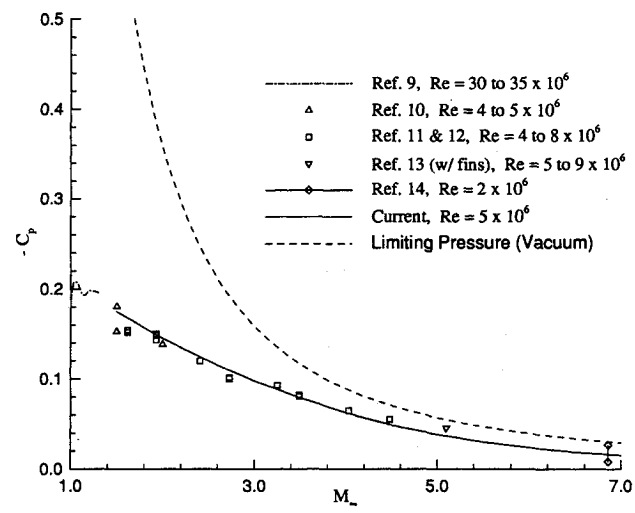

Fig. 20 Base pressure coefficient.

with experiment is again obtained, with the exception of the final station on tip P. The authors have no explanation for this isolated discrepancy.

Separation on the flat nose tip, F3, is visible in the streamlines produced from the current calculations (Fig. 18). The extent of the separation region is approximately 1 caliber. Although separation was not clearly visible in the experimental data, this result agrees both qualitatively and quantitatively with the calculations of Ref. 5.

Cylinder-Flat Base, Turbulent

To establish the validity of the wake region turbulence model, the analysis is done with the base flow isolated from the forebody. The computational model has a small cylindrical section ($\approx 0.05D$) prior to the flat base allowing upstream influence of the corner expansion within the boundary layer. The boundary-layer solution, specified at the inflow boundary of the computational domain, is taken from theory.[24] Upstream of the corner, the modified Baldwin-Lomax model is used. Downstream of the corner, Eq. (12) is implemented. Over the range of Mach numbers, Reynolds number is held fixed at $Re_D = 5 \times 10^5$.

The compiled experimental measurements[9–14] are all for pointed, cylindrical, unfinned bodies with $L/D \approx 10$, and turbulent flow at the body/base corner. The exception is the body in Ref. 13 which had fins and $6.5 \le L/D \le 30$. For all bodies, $Re_L = 2 \times 10^6$ to 9×10^6.

The computed solution at the rearward stagnation point exhibits behavior similar to the forward stagnation point; local aberration in pressure results in an overprediction at the stagnation point. Although some improvement results from using a FD grid type, the pressure still varies across the base an order of magnitude above experimental measurements. By increasing the coefficient in the entropy correction function to 0.85, much better behavior is seen. The base pressure is compared to experiment[31] in Fig. 19. The effect of changing the entropy function on the total or integrated base pressure coefficient is small (about 4%). Therefore, all base flow numerical experiments were conducted with $\varepsilon = 0.85$. It is very important to keep in mind that entropy corrections manifest themselves as additional artificial dissipation in the algorithm. In addition, a universal function does not yet exist, and they remain very geometry dependent. Due to the empiricism of the turbulence model, a more rigorous approach was not attempted.

The integrated pressure coefficient compares very well with the experimental data (Fig. 20). In spite of its empiricism, the wake turbulence model accurately simulates the macroscopic nature of the flow.

Conclusions

The current algorithm represents an efficient implementation of finite-volume methodology, both in terms of computational rate and memory requirement. The general applicability of the method

is validated through the accurate calculation of a wide variety of axisymmetric flow structures: detached bow shocks, recompression shocks (both in the wake and at a separated region near the nosetip), corner-point expansions, base-flow separations and associated recirculations, and turbulent boundary layers. Results are in close agreement with published experimental estimates (within experimental accuracy). The complicated turbulent boudary-layer development is accurately calculated for various nose-tip shapes with a modified Baldwin-Lomax turbulence model. The algorithm's robustness is enhanced by artificially increasing the Reynolds number and controlling the boundary conditions on the base during the initially transient flow development. The effectiveness of this approach is demonstrated by the algorithm's efficiency throughout the range of conditions tested, including the case of a complicated boundary layer/shock interaction associated with the separation near the corner of the flat nosetip.

The results bolster the primary purpose of this investigation: the development and validation of an efficient, accurate, and flexible numerical scheme for the simulation of axisymmetric, high-speed, viscous flows. This work is now the foundation for the construction by the authors of an algorithm for the calculation of fully three-dimensional flows. While completing the study, some notable complexities arose that required the authors to develop important modifications of previously published techniques. These improvements will be reflected in the analyses of three-dimensional flows that the authors are initiating.

Modifications were primarily made to the treatment of singular lines, the wake turbulence model, and the entropy correction function of Yee. An aberration was encountered near stagnation points that is different from the previously documented carbuncle phenomenon. When using non-MUSCL extrapolation to obtain fluxes, a finite-volume grid type (cell interfaces along singular line) accentuated the geometric singularity to produce the aberrant behavior. For the range of tests conducted, a finite-difference gird, used with finite-volume methodology worked well for non-MUSCL extrapolation. An empirical wake region turbulence model was adapted from Ref. 26 for supersonic flow. The simple empirical distribution showed good agreement with the experiments for the considered test cases. The magnitude of the parameter associated with the entropy correction function was much higher for the flat base geometry than the forebody. Further analysis for other types of flux extrapolation and limiter implementation is warranted.

Acknowledgments

The authors would like to thank David Dolling for providing and interpreting the turbulent boundary layer experimental data. The authors also wish to express appreciation to Paul Weinacht and Bernard Guidos at the Army Ballistic Research Laboratory for providing valuable, detailed computational data. Finally, this work was tremendously aided by computer resources provided by Bruce Simpson (Wright Laboratory, Armament Directorate).

References

[1]Anderson, D. A., Tannehill, J. C., and Pletcher, R. H., *Computational Fluid Mechanics and Heat Transfer*, Series in Computational Methods in Mechanics and Thermal Sciences, Hemisphere, New York, 1984, pp. 181–207.

[2]Sturek, W. B., "Application of CFD to the Aerodynamics of Spinning Shell," AIAA Paper 84-0323, Jan. 1984.

[3]Gates, R. S., Winchenbach, G. L., and Cipolla, J. R., "Aerodynamic Test and Analysis of a Slender Generic Missile Configuration," AIAA Paper 89-3368, Aug. 1989.

[4]Vitale, H. E., Winchenbach, G. L., and Riner, W. C., "Aerodynamic Test and Ongoing Analysis of a Slender Generic Missile Configuration," AIAA Paper 91-2895, Aug. 1991.

[5]Guidos, B. J., Weinacht, P., and Dolling, D. S., "Navier-Stokes Computations for Pointed, Spherical, and Flat Tipped Shells at Mach 3," *Journal of Spacecraft and Rockets*, Vol. 29, No. 3, 1992, pp. 305–311.

[6]Kubota, T., "Investigation of Flow Around Simple Bodies in Hypersonic Flow," Graduate Aeronautical Labs., California Inst. of Technology (GALCIT) Hypersonics Wind Tunnel Memorandum No. 40, Pasadena, CA, June 1957.

[7]Dolling, D. S., and Gray, W. K., "Experimental Study of Supersonic Turbulent Flow on a Blunted Axisymmetric Body," *AIAA Journal*, Vol. 24, No. 5, 1986, pp. 793–799.

[8]Guidos, B. J., Weinacht, P., and Dolling, D. S., "Comparison of Navier-Stokes Computations and Experiment for Pointed, Spherical, and Flat Tipped Shells at Mach 2.95," AIAA Paper 90-0587, Jan. 1990.

[9]Hart, R. G., "Effects of Stabilizing Fins and a Rear Support Sting on the Base Pressures of a Body of Revolution in Free Flight at Mach Numbers from 0.7 to 1.3," NACA RM L52E06, 1952.

[10]Chapman, D. R., "An Analysis of Base Pressure at Supersonic Velocities and Comparison with Experiment," NACA Rept. 1051, 1951.

[11]Love, E. S., and O'Donnel, R. M., "Investigations at Supersonic Speeds of the Base Pressure on Bodies of Revolution With and Without Sweptback Stabilizing Fins," NACA RM L52J21a, 1952.

[12]Reller, J. O., and Hamaker, F. M., "An Experimental Investigation of the Base Pressure Characteristics of Nonlifting Bodies of Revolution at Mach Numbers From 2.73 to 4.98," NACA RM A52E20, 1952.

[13]Hill, F. K., "Base Pressures at Supersonic Velocities," *Reader's Forum, Journal of the Aeronautical Sciences*, Vol. 17, No. 3, 1950, pp. 185–187.

[14]Cooper, R. D., and Robinson, R. A., "An Investigation of the Aerodynamic Characteristics of a Series of Cone-Cylinder Configurations at a Mach Number of 6.86," NACA RM L51J09, 1951.

[15]Roe, P. L., "Approximate Riemann Solvers, Parameter Vectors, and Difference Schemes," *Journal of Computational Physics*, Vol. 43, No. 2, 1981, pp. 357–372.

[16]Palmer, G., and Venkatapathy, E., "Effective Treatments of the Singular Line Boundary Problem for Three Dimensional Grids," AIAA Paper 92-0545, Jan. 1992.

[17]Vinokur, M., "An Analysis of Finite-Difference and Finite-Volume Formulations of Conservation Laws," NASA CR 177416, June 1986.

[18]Yee, H. C., "A Class of High-Resolution Explicit and Implicit Shock-Capturing Methods" NASA TM 101088, Feb. 1989.

[19]Harten, A., "High Resolution Schemes for Hyperbolic Conservation Laws," *Journal of Computational Physics*, Vol. 49, No. 3, 1983, pp. 357–393.

[20]Harten, A., Hyman, J. M., and Lax, P. D., "On Finite-Difference Approximations and Entropy Conditions for Shocks," *Communications on Pure and Applied Mathematics*, Vol. 29, No. 3, 1976, pp. 297–322.

[21]Baldwin, B. S., and Lomax, H., "Thin Layer Approximation and Algebraic Model for Separated Turbulent Flow," AIAA Paper 78-0257, Jan. 1978.

[22]Laganelli, A. L., and Dash, S. M., "Turbulence Modeling, Interim Report," Flight Dynamics Lab., Wright Research and Development Center, SBIR AF91-108. Wright-Patterson Air Force Base, OH, July 1990.

[23]Granville, P. S., "A Modified Van Driest Formula for the Missing Length of Turbulent Boundary Layers in Pressure Gradients," *Journal of Fluids Engineering*, Vol. 111, No. 1, 1989, pp. 94–97.

[24]White, F. M., *Viscous Fluid Flow, Second Edition*, McGraw-Hill, New York, 1991, pp. 436–443.

[25]Granville, P. S., "Baldwin-Lomax Factors for Turbulent Boundar Layers in Pressure Gradients," *AIAA Journal*, Vol. 25, No. 12, 1987, pp. 1624–1627.

[26]Magagnato, F., "Computation of Axisymmetric Base Flow with Different Turbulence Models," AGARD CP 493, April 1990, pp. 24-1–24-10.

[27]Steinbrenner, J. P., Chawner, J. R., and Fouts, C. L., "The GRIDGEN 3D Multiple Block Grid Generation System, Volume 1: Final Report," Flight Dynamics Lab., Wright Research and Development Center, WRDC-TR-90-3022, Wright-Patterson Air Force Base, OH, July 1990.

[28]Gabeaud, A., "Base Pressures at Supersonic Velocities," *Reader's Forum, Journal of the Aeronautical Sciences*, Vol. 17, No. 8, 1950, pp. 525, 526.

[29]Josyula, E., Gaitonde, D., and Shang, S., "Nonequilibrium Hypersonic Flow Solutions Using the Roe Flux-Difference Split Scheme," AIAA Paper 91-1700, June 1991.

[30]Dolling, D. S., and Gray, K., "Compilation of Wall Pressure and Turbulent Boundary Layer Data for Supersonic High Reynolds Number Flow Over a Blunted Tangent Ogive Cylinder at Small Angles of Attack," Mechanical and Aerospace Engineering Dept., Princeton Univ., Rept. #1585-MAE, Princeton, NJ, Sept. 1982.

[31]Donaldson, I. S., "The Effects of String Supports on the Base Pressure of a Blunt-Based Body in a Supersonic Stream," *The Aeronautical Quarterly*, Vol. 6, No. 3, 1955, pp. 221–229.

[32]Lin, H., "Dissipation Additons to Flux-Difference Splitting," AIAA Paper 91-1544, June 1991.

[33]Van Leer, B., Thomas, J. L., Roe, P. L., and Newsome, R. W., "A Comparison of Numerical Flux Formula for the Euler Equations and Navier-Stokes Equations," AIAA Paper 87-1104, Jan. 1987.